Research Article Vol. 58, No. 13 / 1 May 2019 / Applied Optics D1

applied optics

Design of a hybrid chalcogenide-glass on lithium-niobate waveguide structure for high-performance cascaded third- and second-order optical nonlinearities

Guillermo Fernando Camacho Gonzalez,[1] Marcin Malinowski,[1] Amirmahdi Honardoost,[1,2] and Sasan Fathpour[1,2,*]

[1]CREOL, The College of Optics and Photonics, University of Central Florida, Orlando, Florida 32816, USA
[2]Department of Electrical and Computer Engineering, University of Central Florida, Orlando, Florida 32816, USA
*Corresponding author: fathpour@creol.ucf.edu

Received 3 December 2018; revised 3 January 2019; accepted 4 January 2019; posted 7 January 2019 (Doc. ID 353400); published 15 February 2019

Dispersion engineering for efficient supercontinuum generation (SCG) is investigated in a hybrid nonlinear photonic platform that allows cascaded third- and second-order optical nonlinearities in transverse-electric (TE) guided modes. The highly nonlinear chalcogenide waveguides enable SCG spanning over 1.25 octaves (from about 1160 nm to more than 2800 nm at 20 dB below maximum power), while the TE polarization attained is compatible with efficient second-harmonic generation in a subsequent thin-film lithium niobate waveguide integrated monolithically on the same chip. A low-energy pump pulsed laser source of only 25 pJ with 250 fs duration, centered at a wavelength of 1550 nm, can achieve such wideband SCG. The design presented is suitable for the f-to-$2f$ carrier-envelope offset detection technique of stabilized optical frequency comb sources.

https://doi.org/10.1364/AO.58.0000D1

1. INTRODUCTION

Supercontinuum generation (SCG) is a process of spectral broadening induced by nonlinear optical effects. It has been used to generate broadband optical frequency combs, which, depending on their spectral domains, can be used in applications such as optical spectroscopy [1], chemical sensing and microscopy [2], microwave photonics [3], astronomic spectrographs [4], and telecommunications [5]. Frequency combs are commonly generated through optical fiber and bulk technologies, although submicrometer integrated photonic waveguides generally possess superior properties for nonlinear effects at shorter lengths and with lower average power budgets. The high index contrast achievable in submicrometer waveguides allows tight mode confinement, giving rise to large electromagnetic fields, and thus enhances the nonlinear effects. This has motivated a growing interest in nonlinear integrated photonics for the optical comb application [6–8]. Future developments could potentially lead to an increment of information rates, all-optical data processing, high-precision metrology, creation of broad spectral sources for on-chip optical spectroscopy, etc.

Optical frequency comb stabilization, by the f-to-$2f$ carrier-envelope offset (CEO) locking technique, requires at least an octave span of SCG and efficient second-harmonic generation (SHG) for CEO signal detection [8]. This implies the use of a highly third-order nonlinear medium to generate a broad frequency comb and a highly second-order nonlinear material for frequency doubling. Furthermore, other applications can be envisioned by involving both nonlinearities, in which broadband phase-matching conditions are fulfilled for SHG, such that a pre-broadened spectrum is extended to shorter wavelengths, resulting in a multi-octave spectrum [9].

Among several material candidates [10], lithium niobate (LN) exhibits very strong second-order optical nonlinearity [$\chi^{(2)}$ susceptibility] for SHG. Recent progress has created an opportunity for using thin films of LN in high-contrast ultra-compact integrated waveguides [11]. To overcome the issue of phase mismatch between the seed and converted guided optical waves, methods such as periodically poled LN (PPLN) [12] and grating-assisted mode-shape modulation [13] can be applied to the high-contrast waveguides.

SCG at telecom wavelengths has been studied in a wide variety of highly third-order nonlinear [$\chi^{(3)}$ susceptibility] materials. SCG spanning over an octave has been demonstrated in silicon nitride (SiN) [14], chalcogenide (ChG) glass [15,16], silicon germanium [17], indium gallium phosphide [18], and silicon [19] waveguides. Even SCG over two octaves has been

reported in SiN [20] and aluminum nitride (AlN) [21]. AlN has the advantage of possessing high amounts of both quadratic and cubic nonlinearities, hence simultaneously achieving SHG and SCG on a single waveguide, and measuring the CEO frequency is feasible. However, both phenomena depend on waveguide dimensions and polarization, so the conditions for SHG may not be ideal for SCG and vice versa.

In this paper, we explore a solution that combines LN and ChG, with strong $\chi^{(2)}$ and $\chi^{(3)}$ nonlinearities, respectively, on a single chip. This cascaded integration, or nonlinear photonic circuit, allows us to optimize the two waveguides segments individually, leading to the desired wide spectrum for SCG and quasi-phase-matching (QPM) for efficient SHG [10], independent of each other.

2. PRECEPTS OF THE HYBRID PLATFORM FOR HIGH-PERFORMANCE CASCADED NONLINEARITIES

The first step toward the discussed nonlinear photonic circuits is to prove not only that integration is feasible between the two materials, but also that the optical energy can be transferred from one to the other. To this end, we decouple a ChG channel waveguide from a thin film of LN using a SiN rib (see the inset in Fig. 1). We have shown experimentally that the optical mode can reside within the ChG waveguide in the first segment and subsequently be transferred via adiabatic tapers into the LN film where it is laterally confined by the SiN rib [22]. In this previous work, we also demonstrated four-wave mixing (FWM) in the ChG waveguide, although the design was not suitable for wideband SCG. In the present paper, we focus on tailoring the structural and dispersion design for over an octave of SCG.

It is generally imperative to understand how the total group-velocity dispersion (GVD) and pump wavelength affect the spectral broadening. Accordingly, if the pump pulse spectrum falls within the waveguide's normal dispersion regime, the broadening mainly originates from self-phase modulation (SPM), and hence will be very limited in extension. Conversely, if the pulse is launched in the anomalous regime, additional broadening phenomena can be involved. Examples are optical Cherenkov radiation (OCR, responsible in dispersive waves), cascaded FWM, modulation instability (MI), cross-phase modulation, and soliton fission, all of which extend the spectral broadening beyond that of the normal dispersion regime [23,24]. It has also been shown that the more anomalous the dispersion, the narrower the bandwidth, and vice versa [25]. Therefore, the total GVD has to be optimized for the pump wavelength to ideally fall in the anomalous regime and stay close to zero in an as large wavelength range as possible.

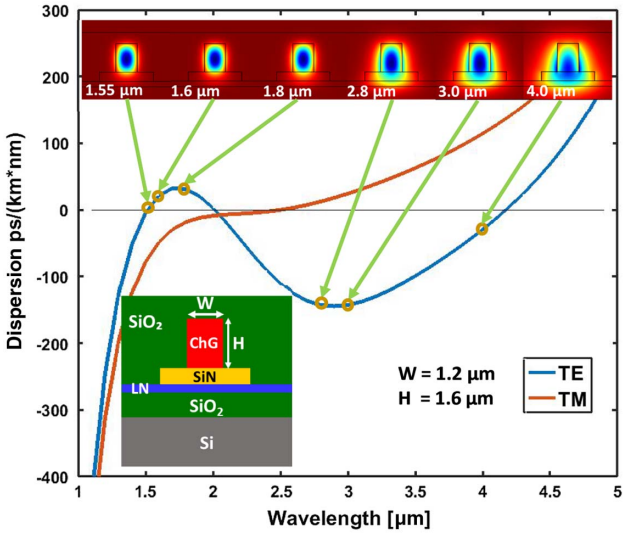

Fig. 1. Detailed mode analysis showing how the inflection points of the GVD arise when the mode is expanded into adjacent regions for TE polarization. TM dispersion is also shown for comparison.

Coherence is another important characteristic to analyze in SCG, given that many applications depend upon it, including optical coherence tomography, ultrashort pulse compression, and high-precision frequency metrology. MI is a spontaneous gain process, such that the stronger it is, the less coherent the supercontinuum (SC). MI grows with input power, propagation length, and in strong anomalous dispersion [26], and is, thus, critical to minimize the impacts of these factors. OCR is a determinant broadening process in the anomalous regime, and it relies on phase-matching conditions only possible across zero-dispersion wavelengths. Accordingly, one-zero dispersion leads to one dispersive wave, two-zero dispersion leads to two-dispersive waves, and so on [24]. Considering that the total GVD is the addition of material and waveguide dispersions, it can be adjusted by either changing the materials involved or by modifying the waveguide structure or dimensions. In one creative design, for instance, attaining four-zero GVD—by adding a low-index slot within the waveguide—has been investigated [27,28]. The concept of four-zero dispersion (FZD) provides a better basis for attaining the phase-matching conditions in OCR than for waveguides with one- or two-zero dispersion wavelengths.

The highest nonlinear coefficient of LN is at the crystalline z axis ($d_{33} = 30$ pm/V), and, hence, maximum conversion efficiency occurs when the electric field of the optical wave is collinear to this axis. Thin-film PPLN devices compatible with the current $\chi^{(2)}$ – $\chi^{(3)}$ integration scheme [22] rely on y-cut LN films, due to ease of electrode fabrication for poling. The direct implication is that the crystalline z axis is horizontally oriented, leading to higher performance for transverse-electric (TE) polarized input light. Therefore, all the simulations presented in this work are for the quasi-TE guided modes.

3. DISPERSION CALCULATIONS

The total GVD is calculated by implementing a fully vectorial simulation in the commercial software COMSOL^{TM}, using its RF module to obtain the effective refractive index, n_{eff}, of the fundamental TE and TM (transversal magnetic) modes for a sweep of wavelengths. The dispersion of different materials can be incorporated directly into the simulation. The model accounts for the dispersion of every material involved. Most material dispersions were input by their Sellmeier equation [29], using the parameters listed in Table 1.

Thin-film SiN was characterized in our laboratory using a prism coupling method and fitting to the following Cauchy's equation:

Table 1. Sellmeier Coefficients for the Materials Involved in the Nonlinear Chip Integration [30–33][a]

Material	A	B_1	$C_1[\mu m^2]$	B_2	$C_2[\mu m^2]$	B_3	$C_3[\mu m^2]$
ChG $Ge_{23}Sb_7S_{70}$	3.627	1.021	0.128	0.999	844.9	0	0
LN ordinary	1	2.673	0.018	1.229	0.059	12.61	474.6
LN extra-ordinary	1	2.980	0.020	0.598	0.066	8.954	416.1
SiO_2	1	0.696	0.005	0.408	0.013	0.897	97.93

[a] $n^2(\lambda) = A + \frac{B_1\lambda^2}{\lambda^2 - C_1} + \frac{B_2\lambda^2}{\lambda^2 - C_2} + \frac{B_3\lambda^2}{\lambda^2 - C_3}$.

$$n(\lambda) = 1.9283 + \frac{0.030385\ \mu m^2}{\lambda^2} - \frac{0.0037931\ \mu m^4}{\lambda^4}. \quad (1)$$

Finally, the GVD is calculated through the second-order derivative of n_{eff} with respect to wavelength, λ, i.e., the dispersion parameter D, expressed by

$$D = \frac{\lambda}{c}\left(\frac{d^2 n_{\text{eff}}}{d\lambda^2}\right), \quad (2)$$

where c is the speed of light in vacuum.

Using the cross section of our previously fabricated nonlinear integrated chip [22] as a starting point, the dimensions of SiN and LN were kept unchanged, whereas the dimension of the ChG waveguide was varied. After an exhaustive analysis of the TE mode evolution in the waveguide structures, we noticed that inflection points in the GVD plot occur when the mode expands to the extent that it occupies adjacent material regions (see Fig. 1). From this attribution, it can be inferred that the slower the transition, the smaller the curvature of the dispersion plot, and, hence, by increasing the dimensions of ChG, the dispersion becomes flatter. This leads to the hint that by adding adjacent high-index sections to the waveguide, the number of inflection points may increase, as it happens in the case of slot waveguides giving rise to FZD [27,28].

In contrast to the dispersion of the TE modes, the TM mode presents normal dispersion at 1.55 μm for these tall structures. However, as discussed above, we are only interested in and aimed at the TE SC for further application involving LN waveguides, which possess the desired close-to-zero dispersion.

We studied the effects of waveguide height variations on the dispersion by fixing the width to 1.2 μm and sweeping the height from 1.0 to 2.2 μm. The taller the waveguides, the more the dispersion pulled into the anomalous regime at shorter wavelengths [see Fig. 2(a)]. Conversely, fixing the height to 1.6 μm and increasing the width results in a flatter GVD, affecting the dispersion mostly around a wavelength of 3 μm, along with a major impact on the trend than height variation [Fig. 2(b)]. This difference is attributed to the nature of the TE mode, which oscillates in parallel to the horizontal axis, hence having more interaction with the side boundaries than with the top and bottom material interfaces. A combination of these effects is used to get the desired GVD with small anomalous dispersion at a wavelength of 1.55 μm, where the input pump will be centered.

In Figs. 2(a) and 2(b), it can be observed that the anomalous dispersion regime cannot be greatly extended into wavelengths below ~1.5 μm by only modifying the ChG dimensions, but it is enough to achieve the desired dispersion profile. Henceforward, we rely on OCR for wide spectrum broadening. However, in the case that further SCG extension to shorter wavelengths is desired, additional modifications can help, i.e., changing the dimensions of SiN and LN or trying different cladding materials.

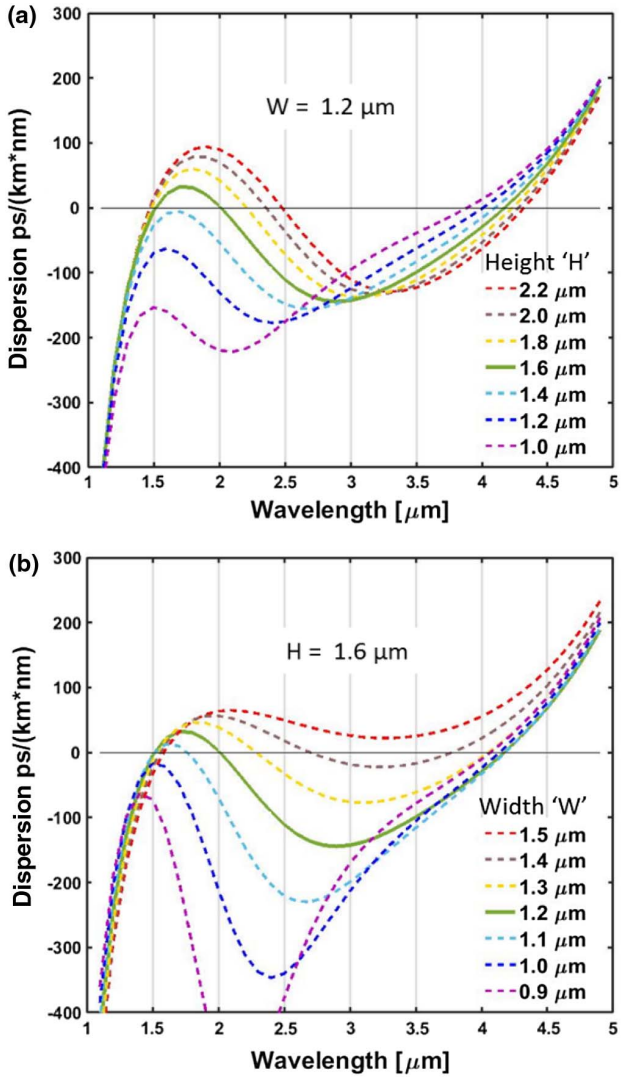

Fig. 2. Dispersion plots for the ChG waveguide by (a) height and (b) width variations. The continuous line in green represents the chosen dispersion for SCG.

To summarize the design, the dimensions for the hybrid waveguides are as follows: a 300 nm thin film of LN on a SiO_2 substrate; a 3-μm-wide, 500-nm-tall SiN rib loaded on LN; and a 1.2-μm-wide, 1.6-μm-tall ChG channel waveguide centered on top of the SiN rib. Under this condition, we get the pump to fall closer to zero dispersion, hence having smaller anomalous dispersion, conditions that lead to a wide SC.

Similar general arguments and tradeoffs have been observed previously in the case of ChG fibers [34].

4. SUPERCONTINUUM SIMULATION

An in-house code that solves the general nonlinear Schrödinger equation (GNLSE) is employed to simulate the SC generated as the input pulse propagates through the waveguide, i.e. [35],

$$\frac{\partial A}{\partial z}+\frac{\alpha}{2}A-\sum_{k\geq 2}\frac{i^{k+1}}{k!}\beta^{(k)}\frac{\partial^k A}{\partial T^k}=i\gamma\left(1+i\tau_s\frac{\partial}{\partial T}\right)|A|^2A, \quad (3)$$

where A is the complex amplitude of the electric field of the optical mode, α is the linear loss coefficient, $\beta^{(k)}$ is the k th-order dispersion, and γ is the nonlinear constant. Also, $T=t-\beta^{(1)}z$ is the time transformed into a moving frame and $\tau_s=1/\omega_0$, where ω_0 is the central angular frequency of the input pulse.

Terms related to the Raman scattering can also be added to Eq. (3) [35]. However, the corresponding parameters have not been measured for the particular ChG composition used in this work; therefore, the associated inelastic nonlinear effects are not included in the simulations. Nevertheless, it is expected that they merely cause a non-critical energy conversion in the resulting spectrum, and not seriously quench the desired elastic $\chi^{(3)}$ effects.

The simulations are adapted to the employed material properties and the estimated technical performances. The propagation loss of the ChG waveguide is set at 1 dB/cm, albeit lower values have been demonstrated in the past [36,37]. Nonlinear absorptions, due to two-photon and free-carrier absorptions, are generally considered negligible for the employed glass composition [30,38]. High-order dispersion parameters were obtained by extending the Taylor series of the calculated second-order dispersion, $\beta^{(2)}=\partial^2(\frac{\omega}{c}n_{\text{eff}})/\partial\omega^2$, i.e.,

$$\beta^{(2)}=\beta^{(2)}(\Omega)+\beta^{(3)}(\Omega)\frac{\Omega}{1!}+\beta^{(4)}\frac{\Omega^2}{2!}+\ldots \quad (4)$$

keeping up to $\beta^{(10)}$, where ω is the angular frequency and $\Omega=\omega-\omega_0$. An expression suitable for high-contrast hybrid waveguides was used for the calculation of γ [39]. That is,

$$\gamma=\frac{2\pi}{\lambda}\left(\frac{n_{\text{eff}}}{n_{\text{core}}}\right)^2\frac{n_2^{\text{avg}}}{A_{\text{eff}}}, \quad (5)$$

where n_{core} is the refractive index of the nonlinear guiding material, A_{eff} is the effective area of the propagating mode, and n_2^{avg} is an average nonlinear refractive index that accounts for all the materials involved. If the nonlinearity is much larger for the core than for adjacent regions, then n_2^{avg} can be approximated as

$$n_2^{\text{avg}}=n_2\frac{n_{\text{core}}^4\int\int_{\text{NL}}|E(x,y)|^4\mathrm{d}x\mathrm{d}y}{\int\int_{-\infty}^{\infty}|E(x,y)|^4n(x,y)^4\mathrm{d}x\mathrm{d}y}, \quad (6)$$

and A_{eff} is calculated as

$$A_{\text{eff}}=\frac{\left(\int\int_{-\infty}^{\infty}n(x,y)^2|E(x,y)|^2\mathrm{d}x\mathrm{d}y\right)^2}{\int\int_{-\infty}^{\infty}n(x,y)^4|E(x,y)|^4\mathrm{d}x\mathrm{d}y}. \quad (7)$$

The nonlinear refractive index of the ChG composition is $n_2=3.71\times10^{-18}$ m^2/W [30], and, thus, the final calculated value of the nonlinear constant is $\gamma=10.53$ W^{-1} m^{-1}. The effective area at the wavelength of 1.55 μm, for instance, is 1.27 μm^2.

The input beam is a sech^2 pulse with a waist of 250 fs full width at half-maximum (FWHM) and peak power of 100 W. This means energy of only 25 pJ, which is adequate for octave-spanning SCG. Indeed, the simulations shown in Fig. 3 confirm that a SC spanning ∼1.27 octaves is feasible with such low-energy pulses, after 40 mm of propagation in the discussed waveguide design. The spectrum extends from ∼1160 to >2800 nm at 20 dB below maximum power. A wider SC output spectrum can be achieved, in principle, by employing shorter-duration input pulses. However, the validity of the employed GNLSE, Eq. (3), becomes questionable for such extremely short pulses [26], and it is thus not explored further here.

In Fig. 3(a), it is clear that the pulse initially broadens symmetrically through SPM. Once it reaches ∼20 mm of propagation length, pulse compression is observed in the time domain [Fig. 3(b)], which leads to rapid spectrum broadening. At this point, dispersive waves become apparent on both sides of the central spectrum; they continue growing with further propagation, pretty much defining the SC limits. After the pulse starts dispersing in time, the optical fields lose their intensity and the spectrum ceases to stretch. This shows the importance of choosing an appropriate waveguide length for the desired functionality. For example, if the waveguide is truncated at 20 mm, a compressed pulse can be attained.

It is also noted that f-to-2f CEO locking is an interference technique, so it requires SCG with decent temporal coherence. Keeping a short propagation distance and low input power are measures to prevent low-coherence broadening effects, such as MI, which is very sensitive to noise, leading to low correlation between consecutive pulses.

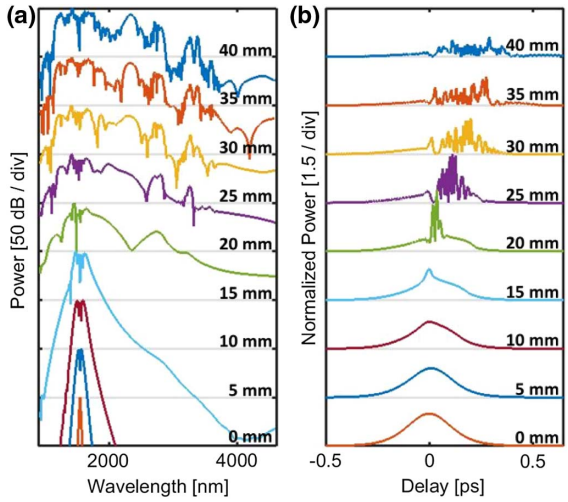

Fig. 3. Pulse evolution in (a) wavelength and (b) time domains after 40 mm propagation of TE modes in hybrid ChG waveguides. It is evident how the pulse starts braking after 15 mm in the time domain, progressing to high compression at 20 mm. The supercontinuum finally extends from ∼1150 to >2800 nm at 20 dB below maximum, i.e., over 1.25 octaves.

5. NONLINEAR HETEROGENEOUS INTEGRATION

The next milestone toward the demonstration of cascaded $\chi^{(2)}$ and $\chi^{(3)}$ nonlinearities is to prove that the optical mode can be transferred efficiently from ChG to LN. This is achievable by careful design of an adiabatic tapered mode converter on the top ChG waveguide, as depicted in Fig. 4(c). As the ChG waveguide is tapered adiabatically, the mode shape evolves continuously, creating a smooth mode translation. The decrease of ChG area leads to a local decrease of the effective refractive index, consequently pushing the mode down to the high-index LN waveguide. We studied the coupling efficiency for a sweep of taper lengths with the use of the commercial software Lumerical MODE Solutions. As presented in Fig. 4(d), we find that keeping the taper length above 100 μm will grant a high coupling efficiency, close to 100%, at an example wavelength of 2.4 μm, corresponding to the long-wavelength tail of the SC spectrum, as required for the f-to-$2f$ CEO detection application. Figure 4(a) shows the mode transition obtained for a 1-mm-long taper. Figures 4(b) and 4(e) are, respectively, the transversal modal cross sections at the beginning and end of the structure layout in Fig. 4(c). The figure shows how the optical mode is initially restrained in ChG and then lands in the LN rib-loaded waveguide, with most of its energy contained in the thin film of LN, where second-order nonlinear processes can occur. As we have shown in our previous work, the discussed tapered mode converters are very broadband [22]. In the present design, the 3 dB bandwidth extends from a wavelength of ∼1.0 μm to above 3.5 μm (not shown).

As shown schematically in Fig. 4(c), the thin film of LN can be periodically poled to achieve QPM [12] and hence high SHG conversion efficiency, for CEO signal detection [8].

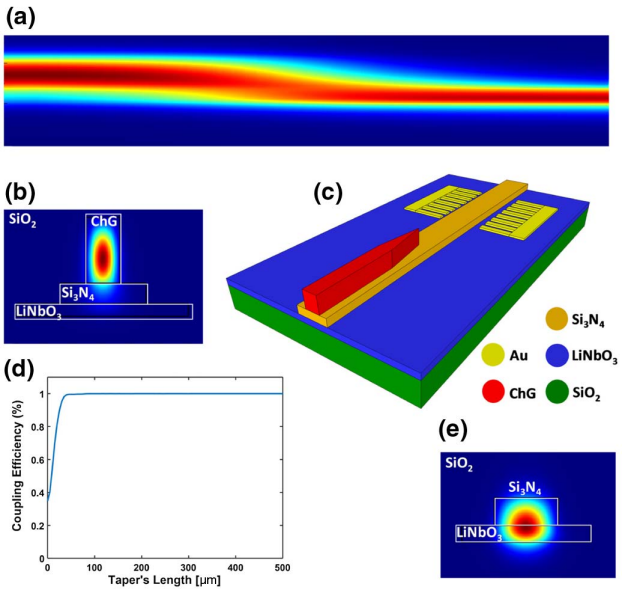

Fig. 4. (a) Quasi-TE optical mode being coupled from ChG to LN. (b) Fundamental mode distribution in the ChG waveguide. (c) A fully integrated nonlinear chip for cascaded $\chi^{(2)}$ and $\chi^{(3)}$ effects. (d) Coupling efficiency through a sweep of taper lengths. (e) Fundamental mode distribution in the LN waveguide.

Another potential application is to engineer the LN poling condition for broad-band QPM, stretching the SC spectrum into shorter wavelengths, potentially with a span of multiple octaves [9].

The fabrication process for the current cascaded nonlinear devices is very similar to our previous experimental work [22]. Starting with a thin film of LN bonded on SiO_2, SiN is deposited on top. The SiN layer is then patterned and etched. Subsequently, a ChG film is deposited, patterned, and etched similarly. Finally, SiO_2 is deposited to passivate the waveguides and attain the complete nonlinear photonic circuit.

6. CONCLUSION

A hybrid nonlinear integrated photonic platform, based on ChG glass and LN materials, is studied for cascading third- and second-order optical nonlinearities, respectively, on the same ultracompact chip. The platform consists of a ChG channel waveguide, separated from a LN thin-film waveguide underneath by a SiN buffer layer. The focus of this paper is to provide design guidelines for dispersion tailoring of ChG waveguides in order to generate TE-polarized SCG spanning over an octave, pumped at ultrashort pulsed sources at telecom wavelengths. Efficient coupling between $\chi^{(2)}$ and $\chi^{(3)}$ devices is also presented, based on carefully designed adiabatic tapered mode converters. The hybrid cascaded nonlinear integrated waveguide platform has potential applications in optical comb generation and frequency stabilization (by the f-to-$2f$ CEO detection method) on a monolithic chip, as well as in multi-octave ultrabroadband sources.

Funding. Defense Advanced Research Projects Agency (DARPA); Consejo Nacional de Ciencia y Tecnología (CONACYT).

REFERENCES

1. F. Keilmann, C. Gohle, and R. Holzwarth, "Time-domain mid-infrared frequency-comb spectrometer," Opt. Lett. **29**, 1542–1544 (2004).
2. C. F. Kaminski, R. S. Watt, A. D. Elder, J. H. Frank, and J. Hult, "Supercontinuum radiation for applications in chemical sensing and microscopy," Appl. Phys. B **92**, 367–378 (2008).
3. C. B. Huang, Z. Jiang, D. Leaird, J. Caraquitena, and A. Weiner, "Spectral line-by-line shaping for optical and microwave arbitrary waveform generations," Laser Photon. Rev. **2**, 227–248 (2008).
4. T. Steinmetz, T. Wilken, C. Araujo-Hauck, R. Holzwarth, T. W. Hänsch, L. Pasquini, A. Manescau, S. D'odorico, M. T. Murphy, T. Kentischer, and W. Schmidt, "Laser frequency combs for astronomical observations," Science **321**, 1335–1337 (2008).
5. S. V. Smirnov, J. D. Ania-Castanon, T. J. Ellingham, S. M. Kobtsev, S. Kukarin, and S. K. Turitsyn, "Optical spectral broadening and supercontinuum generation in telecom applications," Opt. Fiber Technol. **12**, 122–147 (2006).
6. T. J. Kippenberg, R. Holzwarth, and S. A. Diddams, "Microresonator-based optical frequency combs," Science **332**, 555–559 (2011).
7. S. Miller, K. Luke, Y. Okawachi, J. Cardenas, A. L. Gaeta, and M. Lipson, "On-chip frequency comb generation at visible wavelengths via simultaneous second- and third-order optical nonlinearities," Opt. Express **22**, 26517–26525 (2014).
8. A. S. Mayer, A. Klenner, A. R. Johnson, K. Luke, M. R. E. Lamont, Y. Okawachi, M. Lipson, A. L. Gaeta, and U. Keller, "Frequency comb offset detection using supercontinuum generation in silicon nitride waveguides," Opt. Express **23**, 15440–15451 (2015).

9. K. Iwakuni, S. Okubo, O. Tadanaga, H. Inaba, A. Onae, F. L. Hong, and H. Sasada, "Generation of a frequency comb spanning more than 3.6 octaves from ultraviolet to mid infrared," Opt. Lett. **41**, 3980–3983 (2016).
10. A. Rao and S. Fathpour, "Second-harmonic generation in integrated photonics on silicon," Phys. Stat. Solidi A **215**, 1700684 (2018).
11. P. Rabiei, J. Ma, S. Khan, J. Chiles, and S. Fathpour, "Heterogeneous lithium niobate photonics on silicon substrates," Opt. Express **21**, 25573–25581 (2013).
12. A. Rao, M. Malinowski, A. Honardoost, J. R. Talukder, P. Rabiei, P. Delfyett, and S. Fathpour, "Second-harmonic generation in periodically-poled thin film lithium niobate wafer-bonded on silicon," Opt. Express **24**, 29941–29947 (2016).
13. A. Rao, J. Chiles, S. Khan, S. Toroghi, M. Malinowski, G. F. Camacho-González, and S. Fathpour, "Second-harmonic generation in single-mode integrated waveguides based on mode-shape modulation," Appl. Phys. Lett. **110**, 111109 (2017).
14. Y. Okawachi, M. Yu, J. Cardenas, X. Ji, M. Lipson, and A. L. Gaeta, "Coherent, directional supercontinuum generation," Opt. Lett. **42**, 4466–4469 (2017).
15. M. R. E. Lamont, B. Luther-Davies, D. Y. Choi, S. Madden, and B. J. Eggleton, "Supercontinuum generation in dispersion engineered highly nonlinear (γ = 10 /W/m) As_2S_3 chalcogenide planar waveguide," Opt. Express **16**, 14938–14944 (2008).
16. Y. Yu, X. Gai, P. Ma, D. Y. Choi, Z. Yang, R. Wang, S. Debbarma, S. J. Madden, and B. Luther-Davies, "A broadband, quasi-continuous, mid-infrared supercontinuum generated in a chalcogenide glass waveguide," Laser Photon. Rev. **8**, 792–798 (2014).
17. M. A. Ettabib, L. Xu, A. Bogris, A. Kapsalis, M. Belal, E. Lorent, P. Labeye, S. Nicoletti, K. Hammani, D. Syvridis, D. P. Shepherd, J. H. V. Price, D. J. Richardson, and P. Petropoulos, "Broadband telecom to mid-infrared supercontinuum generation in a dispersion-engineered silicon germanium waveguide," Opt. Lett. **40**, 4118–4121 (2015).
18. U. D. Dave, C. Ciret, S. P. Gorza, S. Combrie, A. De Rossi, F. Raineri, G. Roelkens, and B. Kuyken, "Dispersive-wave-based octave-spanning supercontinuum generation in InGaP membrane waveguides on a silicon substrate," Opt. Lett. **40**, 3584–3587 (2015).
19. N. Singh, M. Xin, D. Vermeulen, K. Shtyrkova, N. Li, P. T. Callahan, E. S. Magden, A. Ruocco, N. Fahrenkopf, C. Baiocco, B. P. P. Kuo, S. Radic, E. Ippen, F. X. Kärtner, and M. R. Watts, "Octave-spanning coherent supercontinuum generation in silicon on insulator from 1.06 μm to beyond 2.4 μm," Light Sci. Appl. **7**, 17131–17138 (2018).
20. M. A. G. Porcel, F. Schepers, J. P. Epping, T. Hellwig, M. Hoekman, R. G. Heideman, P. J. M. van der Slot, C. J. Lee, R. Schmidt, R. Bratschitsch, C. Fallnich, and K. J. Boller, "Two-octave spanning supercontinuum generation in stoichiometric silicon nitride waveguides pumped at telecom wavelengths," Opt. Express **25**, 1542–1554 (2017).
21. D. D. Hickstein, H. Jung, D. R. Carlson, A. Lind, I. Coddington, K. Srinivasan, G. G. Ycas, D. C. Cole, A. Kowligy, C. Fredrick, S. Droste, E. S. Lamb, N. R. Newbury, H. X. Tang, S. A. Diddams, and S. B. Papp, "Ultrabroadband supercontinuum generation and frequency-comb stabilization using on-chip waveguides with both cubic and quadratic nonlinearities," Phys. Rev. Appl. **8**, 014025 (2017).
22. A. Honardoost, G. F. Camacho-Gonzalez, S. Khan, M. Malinowski, A. Rao, J. E. Tremblay, A. Yadav, K. A. Richardson, M. C. Wu, and S. Fathpour, "Cascaded integration of optical waveguides with third-order nonlinearity with lithium niobate waveguides on silicon substrates," IEEE Photon. J. **10**, 4500909 (2018).
23. S. Roy, S. K. Bhadra, and G. P. Agrawal, "Effects of higher-order dispersion on resonant dispersive waves emitted by solitons," Opt. Lett. **34**, 2072–2074 (2009).
24. S. Roy, D. Ghosh, S. K. Bhadra, and G. P. Agrawal, "Role of dispersion profile in controlling emission of dispersive waves by solitons in supercontinuum generation," Opt. Commun. **283**, 3081–3088 (2010).
25. Y. Okawachi, M. R. E. Lamont, K. Luke, D. O. Carvalho, M. Yu, M. Lipson, and A. L. Gaeta, "Bandwidth shaping of microresonator-based frequency combs via dispersion engineering," Opt. Lett. **39**, 3535–3538 (2014).
26. G. P. Agrawal, *Nonlinear Fiber Optics* (Academic, 2001).
27. J. Li, K. Xu, and J. Du, "Ultrabroadband and flattened dispersion in aluminum nitride slot waveguides," IEEE Photon. J. **9**, 2700408 (2017).
28. L. Zhang, Q. Lin, Y. Yue, Y. Yan, R. G. Beausoleil, and A. E. Willner, "Silicon waveguide with four zero-dispersion wavelengths and its application in on-chip octave-spanning supercontinuum generation," Opt. Express **20**, 1685–1690 (2012).
29. G. Ghosh, M. Endo, and T. Iwasaki, "Temperature-dependent Sellmeier coefficients and chromatic dispersions for some optical fiber glasses," J. Lightwave Technol. **12**, 1338–1342 (1994).
30. J. W. Choi, Z. Han, B. Sohn, G. F. R. Chen, C. Smith, L. C. Kimerling, K. A. Richardson, A. M. Agarwal, and D. T. H. Tan, "Nonlinear characterization of GeSbS chalcogenide glass waveguides," Sci. Rep. **6**, 39234 (2016).
31. J. E. Tremblay, M. Malinowski, K. A. Richardson, S. Fathpour, and M. C. Wu, "Picojoule-level octave-spanning supercontinuum generation in chalcogenide waveguides," Opt. Express **26**, 21358–21363 (2018).
32. D. E. Zelmon, D. L. Small, and D. Jundt, "Infrared corrected Sellmeier coefficients for congruently grown lithium niobate and 5 mol. % magnesium oxide-doped lithium niobate," J. Opt. Soc. Am. B **14**, 3319–3322 (1997).
33. I. H. Malitson, "Interspecimen comparison of the refractive index of fused silica," J. Opt. Soc. Am. **55**, 1205–1209 (1965).
34. H. Saghaei, M. Moravvej-Farshi, M. Ebnali-Heidari, and M. Moghadasi, "Ultra-wide mid-infrared supercontinuum generation in $As_{40}Se_{60}$ chalcogenide fibers: solid core PCF versus SIF," IEEE Sel. Top. Quantum Electron. **22**, 279–286 (2016).
35. J. M. Dudley, G. Genty, and S. Coen, "Supercontinuum generation in photonic crystal fiber," Rev. Mod. Phys. **78**, 1135–1184 (2006).
36. J. M. Dudley, L. Provino, N. Grossard, H. Maillotte, R. S. Windeler, B. J. Eggleton, and S. Coen, "Supercontinuum generation in air–silica microstructured fibers with nanosecond and femtosecond pulse pumping," J. Opt. Soc. Am. B **19**, 765–771 (2002).
37. J. Chiles, M. Malinowski, A. Rao, S. Novak, K. Richardson, and S. Fathpour, "Low-loss, submicron chalcogenide integrated photonics with chlorine plasma etching," Appl. Phys. Lett. **106**, 111110 (2015).
38. C. Goncalves, M. Kang, B.-U. Sohn, G. Yin, J. Hu, D. Tan, and K. Richardson, "New candidate multicomponent chalcogenide glasses for supercontinuum generation," Appl. Sci. **8**, 2082–2101 (2018).
39. V. S. Afshar, T. M. Monro, and C. M. de Sterke, "Understanding the contribution of mode area and slow light to the effective Kerr nonlinearity of waveguides," Opt. Express **21**, 18558–18571 (2013).